Ocean Engineering xxx (xxxx) 112792

Contents lists available at ScienceDirect

Ocean Engineering

journal homepage: www.elsevier.com/locate/oceaneng

Experimental study of bed evolution around a non-slender square structure under combined solitary wave and steady current actions

Erdinc Sogut [a, 1], Deniz Velioglu Sogut [b], Ali Farhadzadeh [a, *]

[a] Department of Civil Engineering, College of Engineering and Applied Sciences, Stony Brook University, Stony Brook, 11794, New York, USA
[b] Department of Ocean Engineering and Marine Sciences, College of Engineering and Science, Florida Institute of Technology, Melbourne, 32901, Florida, USA

ARTICLE INFO

Keywords:
Non-equilibrium scour
non-slender structure
wave-structure interaction
wave-current interaction
low Keulegan-Carpenter number

ABSTRACT

This paper presents the findings from the laboratory wave flume experiments designed to investigate the formation and evolution of scour around a non-slender, square vertical structure, under three flow conditions, solitary wave, combined solitary wave and steady following current, and combined solitary wave and steady opposing current. The structure was placed on a sandy berm, either fastened to the flume wall or positioned at the centerline of the flume. For the wave only case, the scour on the seaside edge turned out to be deeper than the one on the leeside regardless of the structure's position. The analyses showed that the depth, width, volume, and location of the scour were all significantly influenced by the introduction of steady currents. The following current, for example, deepened the seaside scour, while leading to shallower leeside scour holes as a result of the backfilling process. Contrary to the opposing current, which shifted the scour area in the upwave direction, the scour was transported downwave under the effect of the following current. The scour depth was determined to be a function of the structure position and the Keulegan-Carpenter number, whereas the scour width mostly depended on the structure's position. In this regard, the structure fastened to the wall experienced the widest scour area and the largest volume regardless of the flow condition.

1. Introduction

Coastal structures are exposed to waves and currents, separately or combined. The equilibrium scour around slender cylindrical structures has been thoroughly studied in the specialized literature due to their widespread use in bridge construction and offshore platforms (Harris et al., 2010; Pizarro et al., 2020; Welzel et al., 2019). The first investigations in the literature identified the variables involved in the formation of equilibrium scour around these structures (e.g., monopiles, piers, and pipelines) (Breusers et al., 1977), while providing experimental and analytical results for a large variety of cases (Carreiras et al., 2001; Carrier et al., 2003;Dey et al., 2006, 2011; Kobayashi, 1993; Kobayashi and Oda, 1995; Sumer et al., 1992a, 1992b, 1993, 2007; Sumer, 2007; Sumer and Fredsøe, 2001a, 2001b, 2002; Whitehouse, 1998).

Rance (1980) conducted several experiments to study scour around large monopiles with cylindrical, square, and hexagonal cross-sections under wave or current action. The study showed that the deepest scour was formed around the monopile with square cross-section. Katsui et al. (1993, 1989) and Toue et al. (1993) discovered that the wave-induced steady-streaming was the main driving mechanism of scouring around a large vertical pile under wave action. Kim et al. (1995) investigated the scour around two large cylindrical structures and showed that the scour was a function of structure, wave, and sediment characteristics. Sumer and Fredsøe (2001a) indicated that the scour around a large cylindrical pile was formed due to the suspended sediment, which was, then, transported away from the structure by wave action. They found that the scour depth was a function of both Keulegan-Carpenter number (KC) and diffraction parameter (D/L). Another study by Sumer and Fredsøe (2002) investigated the scour around large square and cylindrical piles, under both wave and combined wave and current flow conditions. They reported that the deepest scour was formed around the square pile, which was consistent with the findings of Rance (1980). The authors argued that the formation of an equilibrium scour around the large cylindrical pile would take longer with increasing Keulegan-Carpenter number and decreasing Shields parameter (θ). Whitehouse (2004) investigated the scour around three different large marine monopile structures. The findings showed that under combined wave and current flow, the foundations

* Corresponding author.
E-mail address: ali.farhadzadeh@stonybrook.edu (A. Farhadzadeh).
[1] *Present Address:* Department of Geology and Geophysics, Woods Hole Oceanographic Institution, Falmouth, 02543, Massachusetts, USA.

https://doi.org/10.1016/j.oceaneng.2022.112792
Received 22 June 2022; Received in revised form 12 September 2022; Accepted 1 October 2022
0029-8018/

were more susceptible to scour and scour protection measures were needed. A study by Haddorp (2005) showed that the scour depth around a pile could be on the order of one and one-third the pile diameter under extreme and moderate wave conditions, respectively. Nakamura et al. (2008) studied the solitary and long wave-induced scour around a square pile. They observed that the maximum scour depth was affected by the relative tsunami wave height and embedded depth of the structure. Qi and Gao (2014) experimentally studied the scour around a large diameter monopile under combined wave and current action. They found that the nonlinear interactions between waves and currents lead to a greater scour depth than that of waves or currents. McGovern et al. (2019) conducted a series of experiments on tsunami waves impinging on a square structure on a flat erodible bed. They discovered that the non-equilibrium scour depth was considerably affected by sediment slumping.

The review of the existing literature reveals that the majority of the studies focused on the equilibrium scour around slender structures resulting in the development of several empirical relationships (Breusers et al., 1977; Raaijmakers and Rudolph, 2008; Sumer et al., 1992a; Sumer and Fredsøe, 2002; Zanke et al., 2011). On the other hand, scour around non-slender, non-cylindrical structures is poorly understood. Flow-induced scouring can potentially contribute or lead to the failure of critical structures during extreme events (Larsen et al., 2017; Williams and Fuhrman, 2016). This entails the investigation of processes associated with scour around beachfront structures during an extreme flooding event—a transient and often non-equilibrium process, where knowledge is still lacking.

The present study investigates the morphological evolution of a sandy berm in the vicinity of a sharp-edged non-slender structure due to the actions of a solitary wave, and combined solitary wave and following/opposing currents at relatively low Keuleguan–Carpenter KCnumbers. Furthermore, the effect of the structure position, attached to the wall and located at the centerline of the flume, on the bed evolution is studied. The non-equilibrium scour characteristics, i.e., depth, width, and volume, as well as the patterns of sediment deposits near the scour area are quantified and described using a set of empirical relationships.

This study is a continuation of the research conducted by the authors (Sogut et al., 2022; Sogut and Farhadzadeh, 2020) which characterizes non-equilibrium scour around non-slender vertical structures of square cross-section under solitary wave action. Here, the authors take a step forward by incorporating the effect of combined flow (waves and currents) on the formation and evolution of non-equilibrium scour. It is believed that the presented data would be a steppingstone for the development of more deterministic approaches to predict non-equilibrium scour around non-slender structures under transient flows.

2. Experiments

The experiments were performed using the integrated wave and bi-directional current flume at Stony Brook University's Coastal and Hydraulic Engineering Research Laboratory (CHERL). The flume which is 25 m long, 1.5 m wide, and 1.5 m high, utilizes a piston-type wet-back wavemaker that is equipped with an active wave absorption system (AWAS). The wavemaker and the flow recirculation system can run together to generate combined wave and current flow conditions. A honeycomb mesh was placed at the end of the wave flume, across from the wavemaker, as a passive wave energy absorption system, to suppress any reflected waves.

The experimental setup consisted of a sharp-edged wooden structure with a square cross-section of 0.50 m × 0.50 m ($D \times D$) placed on a 0.18 m (z_s) thick sandy berm. The median grain diameter of the sand was $d_{50} = 0.27$ mm. The berm was 5.70 m wide and had an approach slope of $m = 1/15$ on both sides. The offshore still water depth (h_0) was 0.48 m, yielding a 0.30 m still water depth on the berm (h). The incident solitary wave had a height of 10 cm (H) in front of the paddle. The steady state current velocity at $h/3$ above the sandy bed (u_c) was 0.15 m/s for the following current and −0.15 m/s for the opposing current. For the combined wave and current tests, the pump was turned on to recirculate the flow in the flume and underneath pipe. It took approximately 1 min for the current to become steady before the wave was generated and propagated along the flume. The steady current was not strong enough to mobilize the sediment in the absence of a wave. The structure was placed at two different positions: (i) attached to the sidewall (side), and (ii) at the centerline (center) of the flume.

2.1. Flow measurement

Prior to placing the structure on the berm, the undisturbed flow field, i.e., the flow field that is not modified by the presence of the structure, was measured using three Edinburgh Designs WG8USB resistive wave gauges (WG), a Nortek Vectrino Acoustic Doppler Velocimeter (ADV), and a Vectrino Profiler at sampling frequencies of 128 Hz, 25 Hz, and 25 Hz, respectively. The profiler recorded the velocity profile over a 3 cm water column at a resolution of 0.1 cm (Fig. 1). The profile of the undisturbed streamwise velocity component (u) on the berm was captured by setting the ADV at different depths and measuring the velocity for an extended period. Furthermore, the undisturbed near-bed streamwise velocity (u_m) profile was recorded between ~2 mm and 32 mm above the berm using the profiler. The coordinates of the WGs, ADV, and profiler are summarized in Table 1.

In the presence of the structure, the disturbed flow field was measured using nine WGs and three ADVs. The positions of the instruments are illustrated in Fig. 2 and their coordinates are summarized in Table 2. The ADVs were set at an elevation of one-third the still water depth ($h/3$)above the bed.

2.2. Bed elevation measurement

The surface of the sandy berm was carefully leveled prior to each test and before the water level was gradually increased to the target still water level. The bed was scanned before and after each test using a HR-Wallingford HRBP-1070 bed profiler system, operating in a three-dimensional setting. The bed profiler was equipped with a laser probe functioning in both air and water, with ±0.5 mm accuracy. At the be-

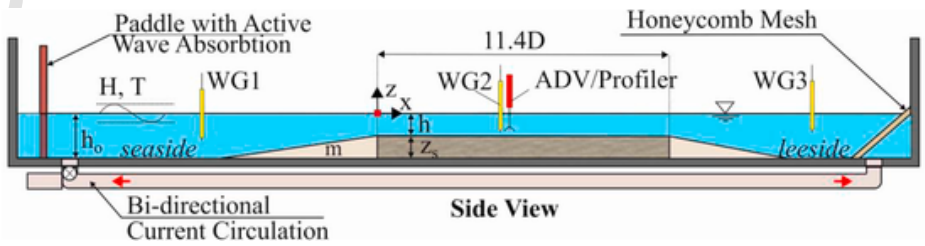

Fig. 1. Schematic of experimental setup (side view) for undisturbed flow measurement. Yellow rectangles represent WGs, red rectangle represents ADV/Profiler. H and T are the incident wave height and period. (For interpretation of the references to color in this figure legend, the reader is referred to the Web version of this article.)

Table 1
Coordinates of WGs, ADV and profiler.

	WG1	WG2	WG3	ADV	Profiler
x/D	−5.20	4.92	11.76	4.95	4.95
y/D	1.50	1.50	1.50	1.50	1.50

ginning of each test, the bed profiler was calibrated to eliminate potential reading errors due to variations in the ambient temperature. The scanned area had a rectangular geometry, $5D$ long and $3D$ wide. The maneuvering restrictions of the probe arm assembly; however, left a ~$0.04D$ wide blind zone around the structure, which had to be measured manually.

2.3. Test case specifications

The functional relationships useful to predict the scour characteristics are expressed as:

$$f\left(S, U, U_f, h_0, h, T, d_{50}, \rho, \rho_s, \mu, g, D\right) = 0 \tag{1}$$

where f represents a function, S is the scour depth, U is the maximum undisturbed/disturbed near-bed velocity, U_f is the maximum shear velocity at the edge of the structure and $U_f = \sqrt{2f_w}\,U$, f_w is the friction factor given in Eq. (7), L is the wavelength, T is the wave period and $T = 3.2$ sec, ρ and ρ_s are the densities of water and sediment, respectively, μ is the dynamic viscosity of water, g is the gravitational acceleration.

The following function (Eq. (2)) is generated using Buckingham's theorem (Buckingham, 1914) of the dimensional analysis and selecting U,ρ, and D as repeating variables.

$$\frac{S}{D} = f\left(KC, Re, \theta, \frac{h_0}{D}, \frac{h}{D}, \frac{d_{50}}{D}, \frac{\rho_s - \rho}{\rho}\right) \tag{2}$$

where KC is the Keulegan-Carpenter number defined as $KC = UT/D$, Re is the Reynolds number, $Re = \rho UD/\mu$, and θ is the Shields parameter given by $\theta = U_f^2/gd_{50}(s-1)$ and $s = \rho_s/\rho$.

The naming convention given in Table 3 reflects the specifications of each test. The letters S and C refer to the side and center positions, respectively. The wave only, combined wave and following current, and combined wave and opposing current flow conditions are referred to as W_0, W_{fc} and W_{oc}, respectively.

In Table 3, u_m^* and u_c^* are the undisturbed near-bed and current velocities on the berm normalized by the shallow water wave celerity, $c = \sqrt{gh}$, respectively. The Reynolds number and Shields parameter are discussed under Sections 3.2.2 and 3.2.4.

3. Results and discussions

In the following subsections, the local hydrodynamics including the free surface elevation and flow velocity under the various flow conditions and structure positions are presented and discussed. The bed evolution and non-equilibrium scour characteristics associated with each test is then analyzed.

3.1. Local hydrodynamics

Fig. 3 illustrates the temporal variations of the free surface elevation ($\eta^* = \eta/H$) in the absence of the structure, normalized by the incident wave height. The wave height at WG1 slightly decreases in the presence of the following current (W_{fc}). On the other hand, for the combined wave and opposing current (W_{oc}), the wave becomes steeper (Velioglu Sogut et al., 2021) such that white capping was observed during the experiment—resulting in a slight reduction of the wave height, captured by WG3. In the presence of the following current, the wave celerity is increased by ~2%–3% — according to the difference between the wave arrival time at WG3. The opposing current, on the other hand, reduces the wave celerity by the same amount, i.e., 2%–3%.

Fig. 4 presents the profiles of the measured instantaneous undisturbed streamwise velocity, u^*, on the berm. Here, the streamwise velocity is normalized by the wave celerity, c. The profiles reveal that the velocity is altered by ±~20% due to the presence of currents (Fig. 4a). Fig. 4d indicates a nonlinear interaction between the wave and current as the magnitudes of the measured and linearly superposed streamwise velocity are not equal. This difference is highlighted in Fig. 4e which shows the maximum streamwise velocity profiles, u^*_{max}, occurring under the wave crest. Fig. 4f shows the differences between the linearly superposed and measured near-bed velocity profiles. The linear superposition leads to an overestimation and underestimation of the flow velocity under the following and opposing currents, respectively.

Fig. 5 shows the temporal variations of the normalized free surface elevations, η^*, in the presence of the structure. The effect of the current on the wave profile is clearly visible closer to the structure where the flow is modulated further by the blockage effect. From the measured

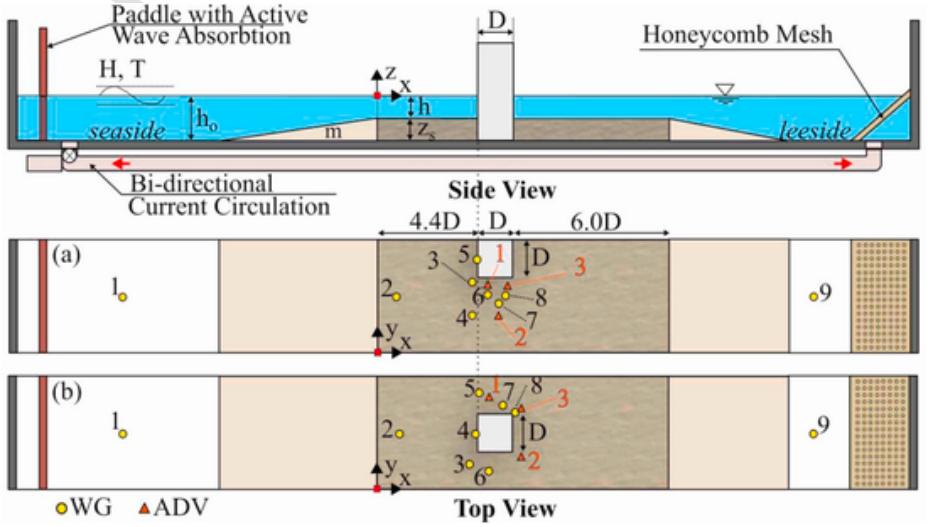

Fig. 2. Schematic of experimental setup with structure (a) on the side and (b) at the center. Yellow circles and red triangles represent WGs and ADVs, respectively. (For interpretation of the references to color in this figure legend, the reader is referred to the Web version of this article.)

Table 2
Coordinates of WGs and ADVs.

Instrument	Side		Center	
	x/D	y/D	x/D	y/D
WG1	−5.20	1.50	−5.20	1.50
WG2	0.70	1.50	0.70	1.50
WG3	4.20	1.90	4.18	0.68
WG4	4.20	1.00	4.36	1.50
WG5	4.36	2.50	4.44	2.60
WG6	4.62	1.56	4.69	0.50
WG7	4.92	1.32	5.07	2.27
WG8	5.10	1.54	5.40	2.07
WG9	11.76	1.50	11.76	1.50
ADV1	4.62	1.84	4.70	2.50
ADV2	4.92	1.02	5.56	0.89
ADV3	5.16	1.80	5.56	2.07

Table 3
Specifications of all test cases.

Test Case	h_0/D	h/D	d_{50}/D	s	u_m^*	u_c^*	KC
$S-W_0$ $C-W_0$	0.96	0.60	5.4×10^{-4}	2.65	0.29	0.00	3.14
$S-W_{fc}$ $C-W_{fc}$	0.96	0.60	5.4×10^{-4}	2.65	0.32	0.09	3.55
$S-W_{oc}$ $C-W_{oc}$	.96	0.60	5.4×10^{-4}	2.65	0.23	−0.09	2.50

wave profile at WG4 that the following current appears to attenuate the wave. The opposing current, on the other hand, reduces the wavelength, resulting in a steepened wave. The flow intensification due to the blockage leads to a noticeable reduction in the wave height for all flow conditions.

The effects of the structure position on the wave runup height are reflected in the instantaneous water level elevations at WG5 and WG4, for the side and center positions, respectively. The runup height on the structure positioned on the side is slightly greater than that of the center position, irrespective of the current direction.

In Fig. 6, the wave runup heights are marked for the two structure positions and different flow conditions. To ease the quantification and comparison of the runup heights, the structure's seaside face is gridded by a $0.2D \times 0.2D$ mesh. For the center position, the wave runs up uniformly across the structure face, whereas the runup on the structure positioned on the side shows a negative gradient towards the channelized flow. The following and opposing currents decrease and increase the wave runup height on the structure located at the center, respectively. A different runup pattern is observed for the side position. This is likely due to the different wave diffraction patterns around the structure when it is placed at two different positions.

The white capping forming due to the introduction of the opposing current slightly reduces the wave height downwave of the structure, which is reflected in the transmitted wave height measured by WG9.

The contaminated raw velocity data of the disturbed flow field was filtered based on signal correlations and Signal-to-Noise Ratio (SNR). The average correlation and SNR values ranged between 7% and 10%, and 85% and 90%, respectively. To visualize the energy distribution across various frequencies of motions in the flow, the Power Spectral Densities (PSDs) of the streamwise flow component, u, were constructed at each ADV location for the two structure positions (Fig. 7). The production range, which is characterized by a -1 slope (Kader and Yaglom, 1991; Katul et al., 1995), represents the low frequency fluctuations in the flow field (e.g. high energy eddies). The inertial subrange has a slope of $-5/3$ (Kolmogorov and Fomin, 1961), where the turbulence kinetic energy (TKE) is transferred from larger eddies to smaller scale eddies. The dissipation range, which contains the eddies of small wave lengths could not be resolved due to the limited sampling frequency of the ADVs. For the low frequency fluctuations, the resolved scales power spectrum density follows the $f^{-5/3}$ scaling. The same trend is not observed for the inertial subrange at the higher frequencies since complex transient flow conditions are dominant due to the presence of the structure.

The temporal variations of the normalized streamwise velocity component, u^*, for the two structure positions and three flow conditions are presented in Fig. 8. The contribution of the steady current to the modulation of the flow velocity in the channelized section of the flume is more significant towards the midpoint of the channel (i.e., at ADV2 for the side position and ADV1 for the center position), compared to the ones closer to the structure.

3.2. Scour characteristics

The combinations of the structure positions and flow conditions lead to different scour patterns around the structure. Fig. 9 illustrates the final bottom elevation, normalized by the structure dimension, (i.e, S/D), for each combination. The scour holes are formed near the sharp edges of the structure, both on the seaside and leeside. In all cases, the footprint of the scour area, characterized by its width, is larger on the leeside than the seaside. The sediment deposits forming on the seaside of the structure are due to the primary vortices that are originated at the sharp edges. These vortices carry the sand as they propagate along a spiral trajectory. The formation and evolution of the primary vortices are discussed in Arabi et al. (2019), Sogut (2021) and Sogut et al. (2020, 2019). Under the wave only flow condition, the sediment deposit is stretched along the channelized flow. However, for the combined wave and flow conditions, the deposits are mostly formed closer to the edges, adjacent to the scour holes. The greatest deposits occur under the combined wave and following current flow condition as shown in the middle panels of Fig. 9. For the combined wave and opposing current, the sediment deposit is more concentrated near the side wall of the structure.

As an outlook of bed evolutions, Fig. 10 depicts the plan views of the final bathymetries shown in Fig. 8. Under the wave only flow condition, the scour depths on the seaside ($0.033D$ for $S-W_0$, and $0.028D$ for $C-W_0$) are greater than those on the leeside ($0.032D$ for $S-W_0$, and $0.023D$ for $C-W_0$). Combining the wave and following current nearly

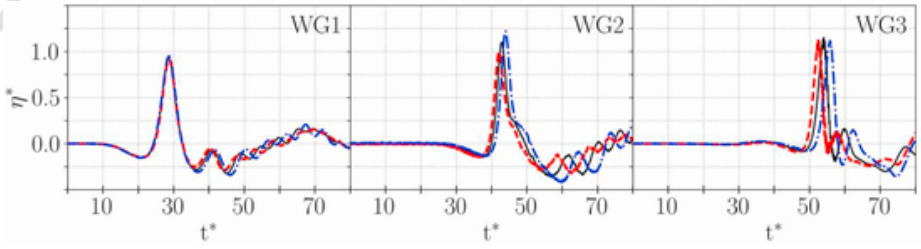

Fig. 3. Temporal variations of normalized free surface elevations with and without steady currents. Black, red, and blue colors represent W_0, W_{fc} and W_{oc}, respectively. $t^* = t\sqrt{g/h}$ is normalized time. (For interpretation of the references to color in this figure legend, the reader is referred to the Web version of this article.)

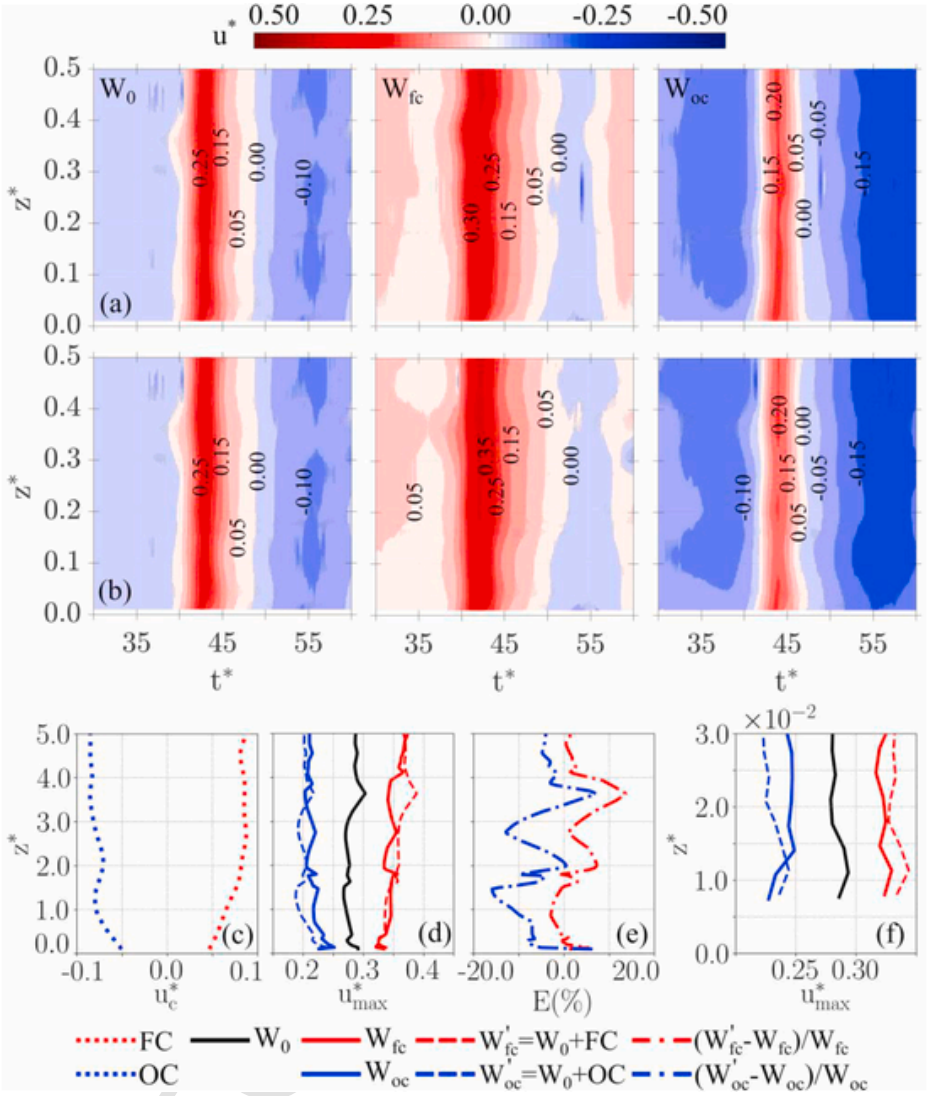

Fig. 4. Temporal variations of (a) normalized measured streamwise velocity (u^*) profiles and (b) linearly superposed wave-following (W'_{fc}) and wave-opposing (W'_{oc}) current cases on the sandy berm. (c) Time-averaged velocity profiles of measured following (FC) and opposing (OC) currents, (d) maxima of measured and linearly superposed streamwise velocity profiles (u^*_{max}), (e) relative difference between linearly superposed and measured velocity profiles and (f) maxima of measured and linearly superposed near-bed velocity profiles. z^* is the normalized vertical coordinate.

doubles the scour depths on the seaside ($0.051D$ for $S-W_{fc}$, and $0.054D$ for $C-W_{fc}$) while the scour depths on the leeside are slightly reduced ($0.030D$ for $S-W_{fc}$, and $0.021D$ for $C-W_{fc}$). The latter is the result of the scour hole backfilling following the transport of the excess sediment removed from the leading edge in the upwave direction. In the case of the combined wave and opposing current, the scour depths on the seaside ($0.022D$ for $S-W_{oc}$, and $0.019D$ for $C-W_{oc}$) are much smaller than those on the leeside ($0.050D$ for $S-W_{oc}$, and $0.055D$ for $C-W_{oc}$), reflecting a pattern contradicting that of the combined wave and following current case.

The traces of the sediment deposits are oriented ~45° with respect to the incident wave direction under the wave only flow condition, consistent with the trajectories of the wake vortices marked in Fig. 10 by the dotted arrows. The wake vortices forming at the sharp edges suspend and entrap the sediment. These migrating wake vortices then carry the suspended sediment away and release them along their trajectories. As a result, the scour holes are formed at the leeside edges, and the sediment is deposited along the vortices' spiral trajectories. The radius of the trajectory is greater for $S-W_{fc}$ compared to that of $S-W_0$. This is due to a higher flow velocity intensification under W_{fc}. Although the intensified flow generates a much stronger wake vortex, the vortex trajectory for $S-W_{fc}$ is shorter than that of $S-W_0$ because the current flow impedes the wake vortex to migrate further in the upwave direction. The opposing current, on the other hand, reduces the intensity of the wake vortices and also bends their trajectory towards the structure's side wall, forming a thin layer of sediment deposit along the trajectory. Unlike $S-W_{fc}$, the trajectories of the wake vortices for $C-W_{fc}$ are not spiral. Consequently, the suspended sand particles entrapped in the core of the wake vortices are transported and deposited downwave as the vortices are weakened. The wake vortices associated with $C-W_{oc}$ are the weakest among all cases. The trajectories are pushed closer to the structure—similar to that of the side position, $S-W_{oc}$. Thus, the sediment entrapped in the core of the vortices is released along the structure's side walls.

Fig. 11 illustrates the cross-sectional views of the normalized final bed elevation, S/D, at the edge and centerline of the structure in the lateral direction. It should be noted that for the center position, C–C represents the average bed elevations along the cross-sections a-a and b-b. At the centerline, no noticeable change in the bed was observed for all cases (Fig. 11a, B–B, and Fig. 11b, D-D). At the edge, on the other hand, the presence of the steady current alters the scour depth, width, and location (Fig. 11a, A-A, and Fig. 11b, C–C).

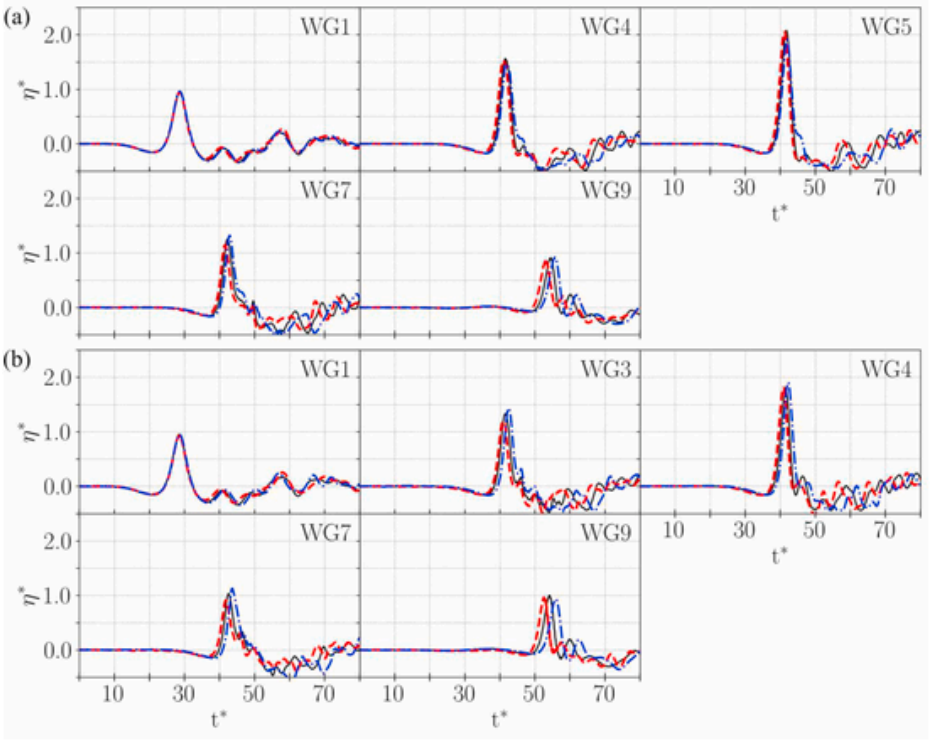

Fig. 5. Spatial and temporal variations of the normalized free surface elevations along the wave flume with and without steady currents for: (a) side and (b) center positions. Black, red, and blue colors represent wave only, wave-following, and wave-opposing current cases, respectively. (For interpretation of the references to color in this figure legend, the reader is referred to the Web version of this article.)

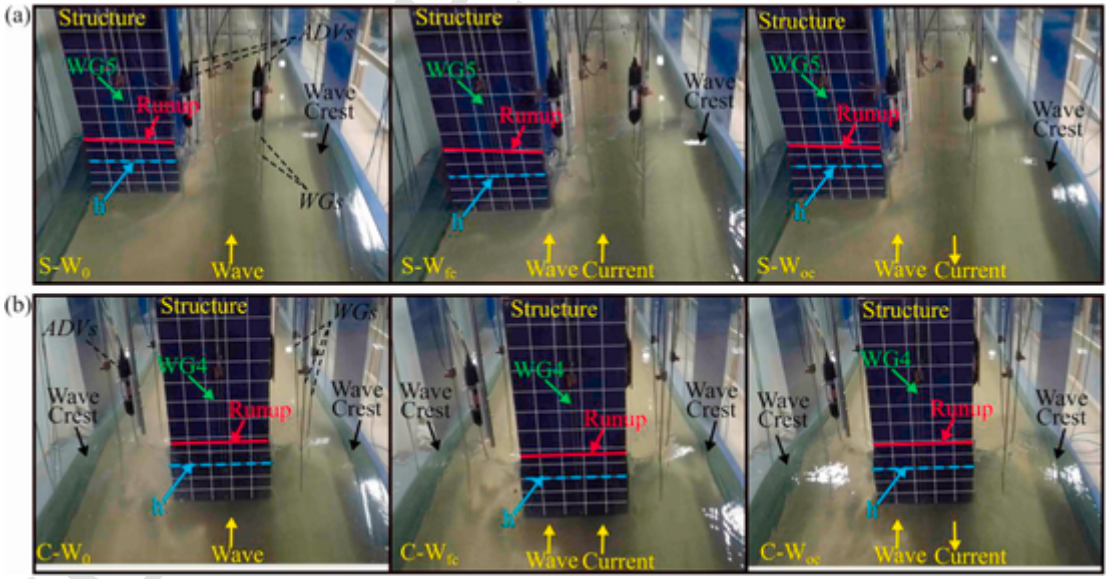

Fig. 6. Wave runup on seaside face of structure for: (a) side and (b) center positions for various flow conditions.

The following current slightly widens the scour holes on both seaside and leeside of the structure, and shift them in the downwave direction (Fig. 11a, A-A). On the other hand, under the effect of the opposing current, the seaside scour depth considerably decreases while the scour on the leeside is deepened. Moreover, the scour area is shifted in the upwave direction. The scour holes for $S-W_{oc}$, are significantly wider than those for $S-W_0$ and $S-W_{fc}$.

Fig. 12 shows the normalized average width of the scour zone normalized by the structure dimension, R_a/D, for various structure positions and flow conditions. The magnitudes of R_a/D on the seaside and leeside of the structure for $S-W_0$, are ~25% greater than those for $C-W_0$. For the combined wave and following current cases, $S-W_{fc}$ and $C-W_{fc}$, the R_a/D values on the seaside edges are ~26% and ~37% greater than those for $S-W_0$ and $C-W_0$, respectively. The magnitudes of R_a/D on the leeside, on the other hand, are ~16% and ~33% smaller for $S-W_{fc}$ and $C-W_{fc}$, respectively. Contrary to the combined wave and following current flow, the opposing current results in a seaside scour width reduction by ~13% and ~21% for $S-W_{oc}$ and $C-W_{oc}$, respectively. The magnitudes of R_a/D on the leeside are ~8% and ~20% greater than those for $S-W_{oc}$ and $C-W_{oc}$, respectively.

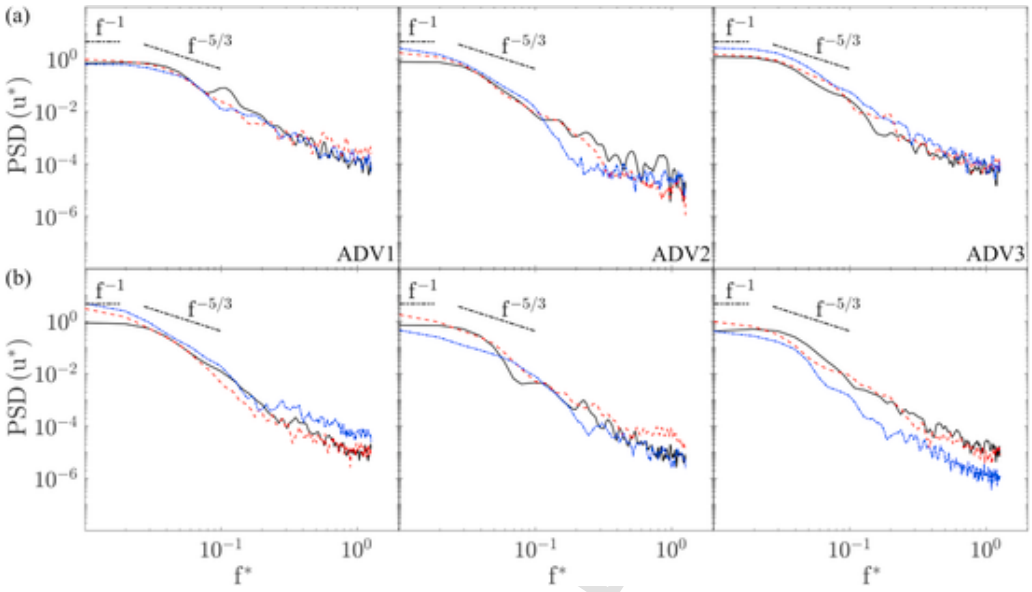

Fig. 7. Comparisons of PSDs for filtered measured streamwise velocities at ADV1, ADV2 and ADV3 for: (a) side and (b) center positions. Black, red, and blue colors represent wave only, wave-following, and wave-opposing current cases, respectively. (For interpretation of the references to color in this figure legend, the reader is referred to the Web version of this article.)

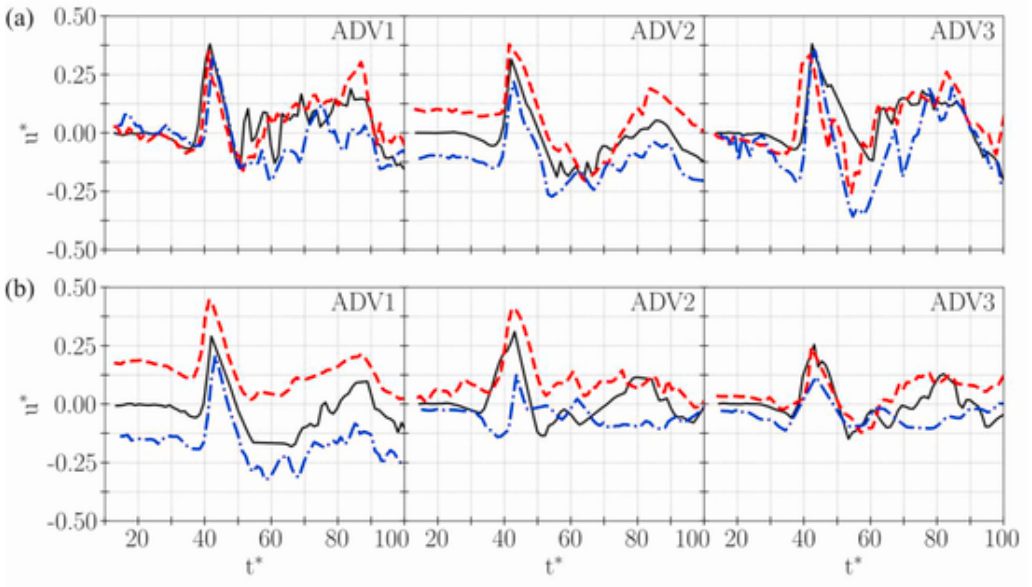

Fig. 8. Temporal variations of the normalized streamwise velocity with and without currents for: (a) side and (b) center positions. Black, red, and blue colors represent wave only, wave-following, and wave-opposing current cases, respectively. (For interpretation of the references to color in this figure legend, the reader is referred to the Web version of this article.)

3.2.1. Blockage effect on near-bed flow velocity

As described above, the presence of the structure alters the local hydrodynamics and consequently the morphology of the sandy bed. The blockage effect for the scour problem is generally disregarded when the blockage ratio, defined as the ratio of the projected width of the structure perpendicular to the incident wave to the channel width (B_R), is less than 1/6 (Whitehouse, 1998). Here, the blockage exceeds the recommended threshold and thus it is considered in the following analyses.

It is also important to reduce the potential effects of the proximity of the flume walls on the experiment. Blockage effects by large structures relative to the flume width in small-scale flume tests could lead to accelerated flow through a decreased cross-sectional area, resulting in contraction scour. Some researchers specified the geometric ratios needed to ensure that blockage effects on scour depth are negligible (Chiew, 1984; Kader et al., 2002; Whitehouse, 1998; Ballio et al., 2009). The proximity of the structure to a wall may also impact the tests, causing flow acceleration and changes to the wake structure. Based on potential flow theory, Sumer and Fredsøe (1997) concluded that the wall effect is negligible when a structure is located at a distance equivalent to its dimension away from the wall for wave flows, and one-to-two times its dimension away from the wall for current flows. Hence, the blockage ratio of the current experimental setting is not expected to have a major impact on the local hydrodynamics. Regardless, the blockage effect is quantified and incorporated in the analysis as described in the following.

Eq. (3) is adopted to establish a relationship between the normalized maximum disturbed ($u^*_{x,m}$) and undisturbed ($u^*_{x,u}$) flow velocity

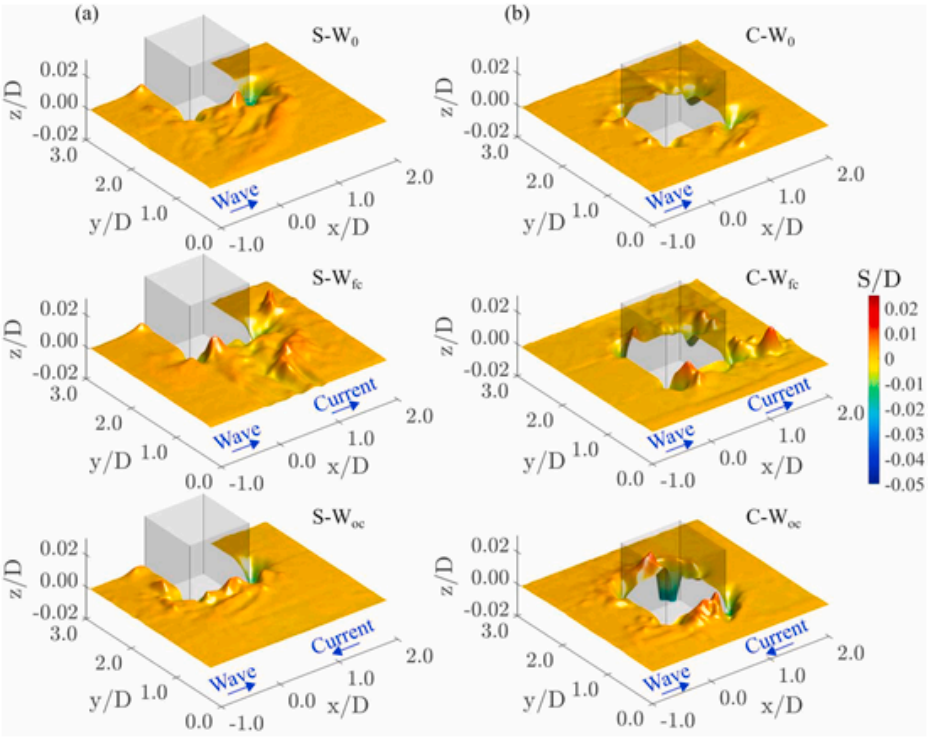

Fig. 9. Three-dimensional view of the normalized bed elevation variation (S/D) for (a) side, and (b) center positions.

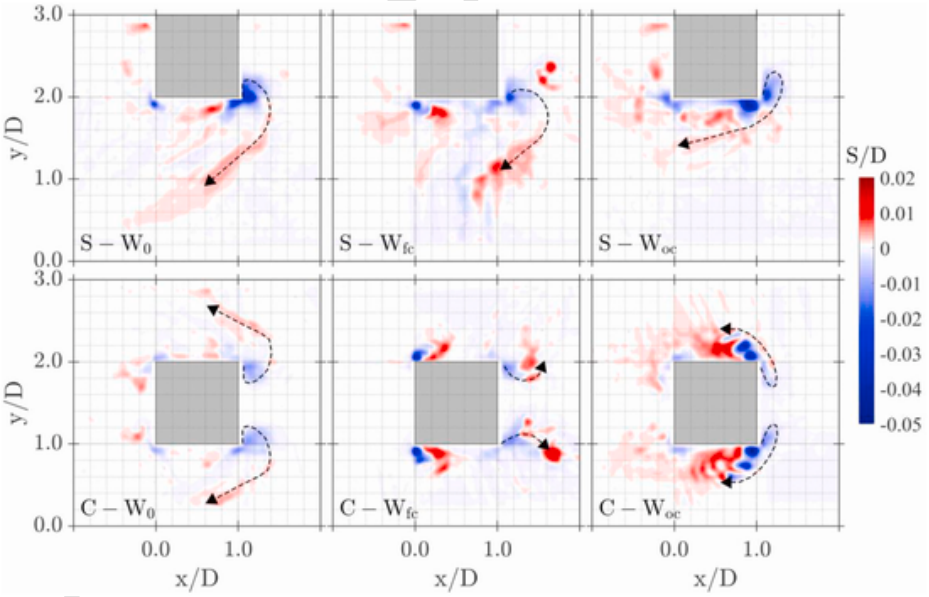

Fig. 10. Plan view of normalized bed level variation (S/D) as well as trajectories of wake vortices, for each test case.

(Sogut et al., 2022). The flow velocities are measured at one-third the still water depth from the bed. Fig. 13a illustrates the relative positions of the ADVs for the $u^*_{x,u}$ and $u^*_{x,m}$ measurements.

$$\frac{u^*_{x,p}}{u^*_{x,u}} = 0.1224\,(B_R) + 1.00 \quad for \quad B_R \le 1/3 \tag{3}$$

where $u^*_{x,p}$ is the predicted normalized maximum disturbed velocity.

As stated in Sogut et al. (2022), the maximum disturbed near-bed velocity (u^*_{mm}) and $u^*_{x,m}$ are assumed to respond similarly to the blockage effect. The measured maximum undisturbed velocity, u^*_m, and modified (disturbed) velocity, u^*_{mm}, are employed for the analyses of the scouring on the seaside and leeside of the structure, respectively. Table 4 summarizes these velocities and the corresponding KC values. As reflected in Table 4, the flow blockage results in a ~4.1% increase in the velocity on the leeside of the structure.

3.2.2. Flow regime

The sediment transport is driven by the shear stresses within the boundary layer. Wave boundary layers are typically thinner than current boundary layers, resulting in higher shear stresses. Under combined wave-current flows, on the other hand, the boundary layer thickness may vary, significantly altering the sediment transport mechanism. The Reynolds number is commonly used to characterize the flow

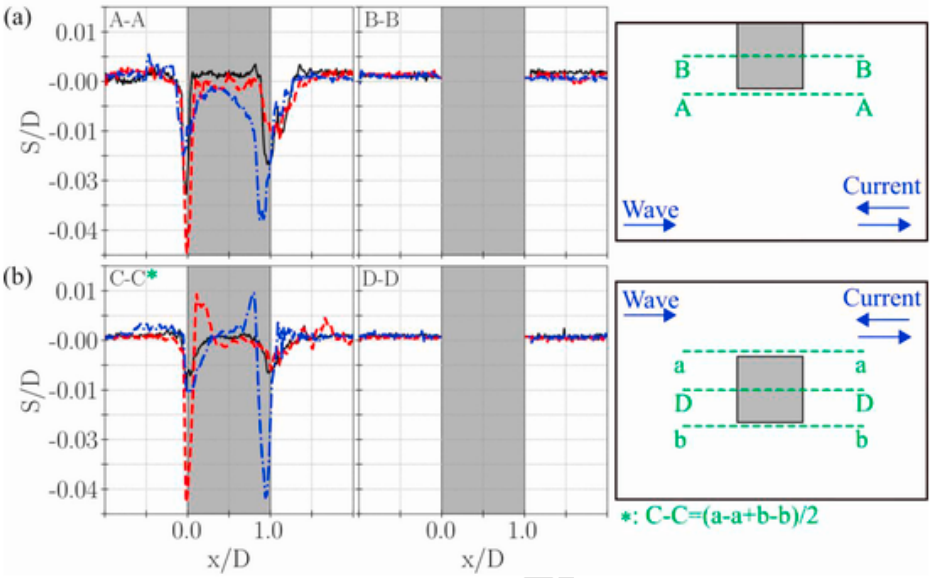

Fig. 11. Cross-sectional views of normalized bed level variation (S/D) for (a) side (b) center positions. Black, red and blue colors indicate wave only, wave-following, and wave-opposing current cases, respectively. (For interpretation of the references to color in this figure legend, the reader is referred to the Web version of this article.)

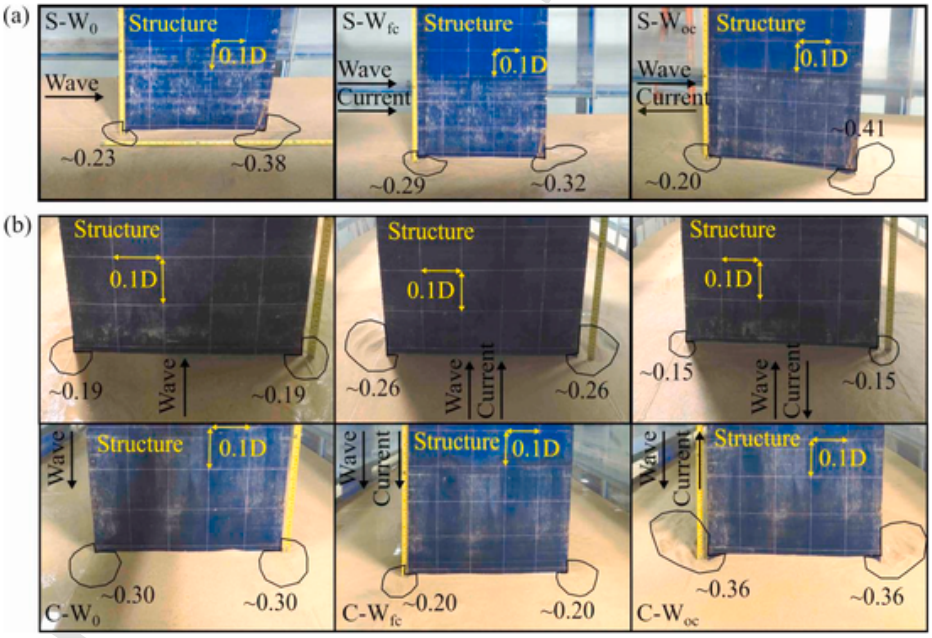

Fig. 12. Footprints of scour holes (R_a/D) for: (a) side and (b) center positions.

regime within a boundary layer. To that end, the equation for the solitary wave boundary layer, proposed by Sumer and Fuhrman (2020) has been adopted here. The equation is valid for a hydraulicly smooth bed and can be utilized as an approximation for other regimes (Sogut et al., 2022). The Reynolds number of a solitary wave boundary layer is given as

$$Re = \frac{aU}{\upsilon} \tag{4}$$

where $U = u_m$ or u_{mm}, υ is the kinematic viscosity of water and $\upsilon = 10^{-6}$ m^2/s, and a is the free stream amplitude, given by

$$a = \frac{UT}{2\pi} \tag{5}$$

The boundary layer transitions from laminar to turbulent when the Reynolds number is greater than 2×10^5 (Carstensen et al., 2010; Fredsøe and Deigaard, 1992; Fuhrman et al., 2009a, 2009b; Sumer et al., 2010).

The behavioral mode of the sandy bed can be described by the roughness Reynolds number, R_e^*, as

$$R_e^* = k_N U_f / \upsilon < 5 \tag{6}$$

where k_N is the Nikuradse roughness which is selected as $k_N = 2.5D_{50}$ following Soulsby (1997) and Sumer et al. (2007) and $U_f = \sqrt{2f_w}\, U$ with f_w being (Fuhrman et al., 2013; Sumer and Fuhrman, 2020):

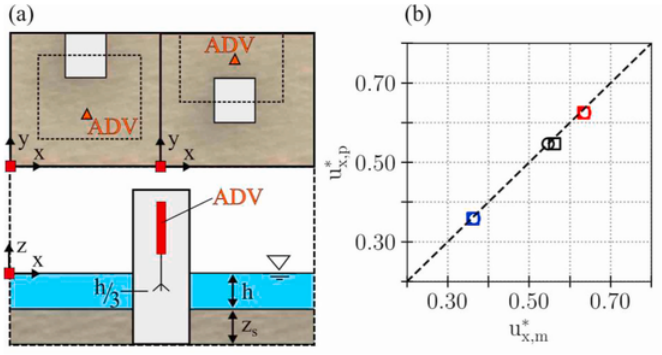

Fig. 13. (a) Positions of ADVs used to assess the blockage effect on flow velocity. (b) Comparisons of normalized predicted $(u^*_{x,p})$ and measured $(u^*_{x,m})$ streamwise velocity components for all test cases. Circles and squares represent side and center positions, respectively. Black, red and blue colors indicate wave only, wave-following, and wave-opposing current cases, respectively. (For interpretation of the references to color in this figure legend, the reader is referred to the Web version of this article.)

Table 4
Maximum near-bed velocities and corresponding *KC* values.

	Seaside		Leeside		
Test Case	u^*_m	KC	u^*_{mm}	KC	$\lvert u^*_{mm} - u^*_m \rvert / u^*_m$
S − W_0 C − W_0	0.29	3.14	0.30	3.27	0.041
S − W_{fc} C − W_{fc}	0.32	3.55	0.34	3.70	0.041
S − W_{oc} C − W_{oc}	0.23	2.50	0.24	2.60	0.041

$$f_w = \exp\left[5.5\left(\frac{a}{k_N}\right)^{-0.16} - 6.7\right] \tag{7}$$

In general, the dimensionless parameter a/k_N (Carstensen et al., 2010; Fuhrman et al., 2009a, 2009b; Sumer et al., 2010; Sumer and Fuhrman, 2020) is used to define friction factor for hydraulically rough ($R^*_e > 70$) or transitional regimes ($5 < R^*_e < 70$).

The magnitudes of Re and R^*_e are given in Table 5. The boundary layer on either side of the structure is identified as laminar and the sandy berm is classified as a hydraulically transitional boundary.

3.2.3. Correlating scour characteristics with Keulegan–Carpenter number

Fig. 14 illustrates the variations of the maximum scour depth, $(S/D)_{\max}$, width, R_a/D, and volume (V_a) as a function of KC. The scour volume is calculated by assuming a cone-shaped hole with a height of $(S/D)_{\max}$ and a base diameter of R_a/D. The magnitude of $(S/D)_{\max}$ is greater for the side position than that of the center position for $KC < \sim 3$. For $KC > \sim 3$, the $(S/D)_{max}$ trend has the steepest slope for the center position. The measured R_a/D and V_a for the side position are greater than those of the center position, for all the KC values. The leeside scour is deeper for the center position than that for the side position, for $KC < \sim 3$. On the other hand, the leeside scour for the center position becomes drastically shallower than that for the side position as KC increases beyond ~3. The maximum scour depths on the seaside and leeside are found to follow the positive (Eq. (8)) and negative (Eq. (9)) power functions with respect to KC, respectively.

Table 5
Summary of flow regime in solitary wave boundary layer for all test cases.

	Seaside				Leeside			
Test Case	a/k_N	R^*_e	Re (× 10^4)	f_w (× 10^{-2})	a/k_N	R^*_e	Re (× 10^4)	f_w (× 10^{-2})
S − W_0 C − W_0	369.9	23.9	12.3	1.04	386.4	24.8	12.8	1.03
S − W_{fc} C − W_{fc}	418.8	26.5	15.7	0.09	437.4	27.5	16.4	0.09
S − W_{oc} C − W_{oc}	294.4	19.8	7.8	1.13	307.5	20.5	8.1	1.11

$$(S/D)_{\max,seaside} = \begin{cases} 0.002KC^{2.57}, & \text{side position} \\ 0.001KC^{3.57}, & \text{center position} \end{cases} \tag{8}$$

$$(S/D)_{\max,leeside} = \begin{cases} 0.23KC^{-1.62}, & \text{side position} \\ 1.99KC^{-3.63}, & \text{center position} \end{cases} \tag{9}$$

Furthermore, the scour width and volume follow ascending and descending trends with respect to KC for the seaside and leesideedges, respectively—consistent with the scour depth.

Fig. 15 shows the generalized relationships, correlating the normalized maximum seaside and leeside scour depths with the KC values for the side and center positions combined. Overall, irrespective of the structure position, the maximum scour depth on the seaside increases with KC, whereas the maximum scour depth on the leeside shows a descending trend—reflected in the magnitudes of the power in the relationships below (Eq. (10)).

$$(S/D)_{\max} = \begin{cases} 0.001KC^{3.02}, & \text{seaside} \\ 0.64KC^{-2.56}, & \text{leeside} \end{cases} \tag{10}$$

3.2.4. Correlating scour characteristics with Shields parameter

The experiments were conducted under clear-water conditions and wake vortices were identified as the main driving mechanism of the scour. These vortices entrap and transport most of the suspended sediment particles along their trajectories. Hence, the Shields parameter is employed to characterize the sediment movement. The dimensionless grain size (D_*) and the associated critical Shields parameter (θ_{cr}) are the two important factors often used to describe the particle suspension threshold (Soulsby, 1997; Soulsby and Whitehouse, 1997; Whitehouse, 1998). In their previous studies (Sogut, 2021; Sogut et al., 2022; Sogut and Farhadzadeh, 2020), the authors determined $D_* = 6.83$ and $\theta_{cr} \approx 0.04$ for the exact same sandy bed.

Sumer et al. (2007) proposed the following equation to determine whether the sediment particles are entrapped and transported by wake vortices

$$\theta_s = \left(\frac{U_f d_{50}}{\upsilon}\right)^{-0.05}\left[0.7\ \exp\left(-0.04\frac{U_f d_{50}}{\upsilon}\right)\right] + 0.26\left[1 - \exp\left(-0.025\frac{U_f d_{50}}{\upsilon}\right)\right] \tag{11}$$

where θ_s is the critical Shields parameter for the suspended sediment entrapment. The suspended sediment is entrapped and transported by a wake vortex when $\theta > \theta_s/4$ (Sumer et al., 2007).

Table 6 depicts the variation of θ, θ_s and θ/θ_s on both sides of the structure. The sediment particles on both sides are suspended and entrapped by the vortices ($\theta > \theta_s/4$) in all test cases.

4. Conclusions

This study presents the results of an experimental investigation focusing on the characteristics of the scour around a vertical non-slender structure with a square cross-section under combined wave and current action. The analyses showed that the linearly superposed wave and current velocity could result in either overestimation or underestimation of the flow velocity depending on the flow direction. For the wave only case, the scour depth on the seaside of the structure was found to be

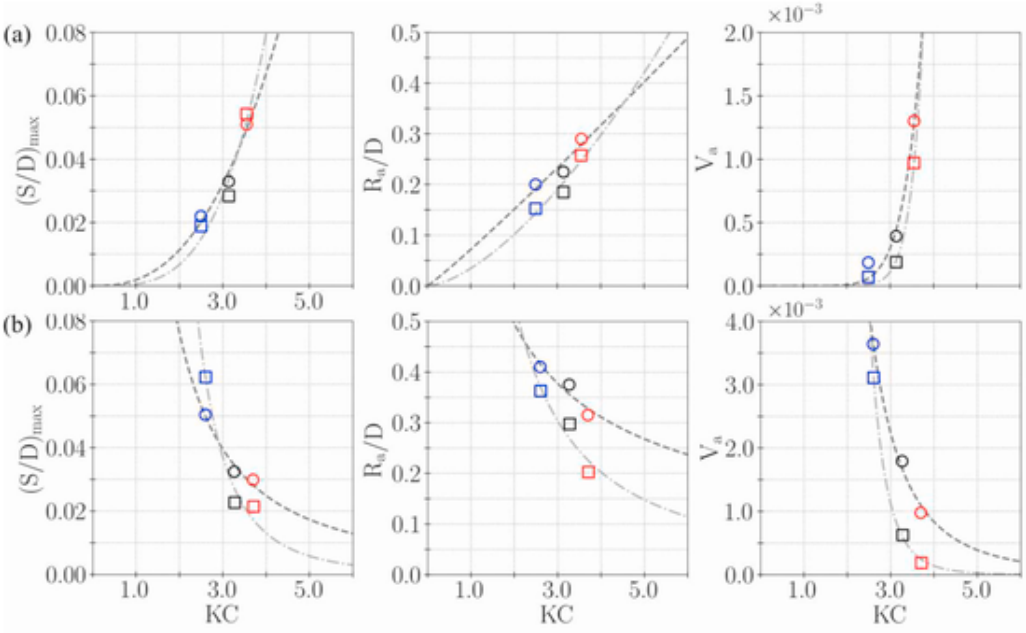

Fig. 14. Variations of $(S/D)_{\max}$, R_a/D and V_a with respect to KC on (a) seaside and (b) leeside of the structure for both positions. Circles and squares represent side and center positions, respectively. Black, red and blue colors indicate wave only, wave-following, and wave-opposing current cases, respectively. Dashed and dash-dotted curves represent side and center positions, respectively. (For interpretation of the references to color in this figure legend, the reader is referred to the Web version of this article.)

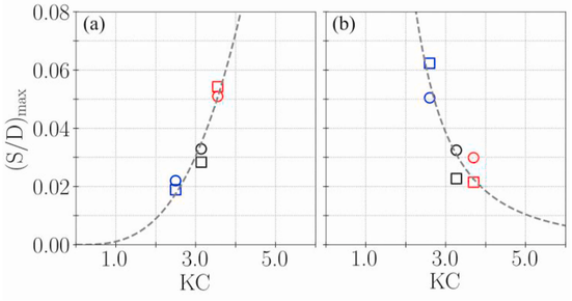

Fig. 15. Variations of $(S/D)_{\max}$ with respect to KC on (a) seaside and (b) leeside of the structure for two positions combined. Circles and squares represent side and center positions, respectively. Black, red and blue colors indicate wave only, wave-following, and wave-opposing current cases, respectively. Dashed line represents the fitted curves. (For interpretation of the references to color in this figure legend, the reader is referred to the Web version of this article.)

Table 6
Variation of θ, θ_s and θ/θ_son seaside and leeside of structure.

Test Case	Seaside			Leeside		
	θ	θ_s	θ/θ_s	θ	θ_s	θ/θ_s
S – W_0 C – W_0	0.287	0.380	0.76	0.308	0.374	0.82
S – W_{fc} C – W_{fc}	0.352	0.364	0.97	0.379	0.359	1.06
S – W_{oc} C – W_{oc}	0.196	0.409	0.48	0.211	0.403	0.52

greater than that on the leeside, irrespective of the structure position across the channel width. The introduction of the steady currents lead to a drastic alteration of the scour patterns and characteristic and the resulting sediment deposits forming around the structure. The scour was deeper on the seaside and shallower on the leeside—due to the sediment backfilling—when the following current was combined with the wave. The position of the scour hole was shifted downwave by the following current, whereas the opposing current lead to an upwave migration of the scour. The steady currents were shown to influence the average width of the wave-induced scour holes on both seaside and leeside. Positioning the structure on the side lead to a greater scour width and volume, irrespective of the flow condition. Empirical relationships for the maximum scour depth on the seaside and leeside of the structure as a function of KC were developed. These relationships showed positive and negative power trends with KC for the seaside and leeside scour depths, respectively.

The findings of this study are limited to the flow conditions, structure size, and positions considered. A more comprehensive study encompassing a wider range of flow conditions, positions, and structure dimensions needs to be considered for conclusive results regarding the scour around non-slender square structures under the combined wave and current cases.

Uncited references

Dey et al., 2011, Dey et al., 2006.

CRediT authorship contribution statement

Erdinc Sogut : Data curation, Formal analysis, Visualization, Writing – original draft. **Deniz Velioglu Sogut :** Writing – review & editing, Writing – original draft. **Ali Farhadzadeh :** Writing – review & editing, Conceptualization, Methodology, Supervision.

Declaration of competing interest

The authors declare that they have no known competing financial interests or personal relationships that could have appeared to influence the work reported in this paper.

Data availability

Data will be made available on request.

Acknowledgments

The authors acknowledge funding from the National Sciences Foundation through grant CMMI-2050798 and The New York State Department of Environmental Conservation, under Award No. 77362.

References

Arabi, M.G., Velioglu Sogut, D., Khosronejad, A., Yalciner, A.C., Farhadzadeh, A., 2019. A numerical and experimental study of local hydrodynamics due to interactions between a solitary wave and an impervious structure. Coast. Eng. 147, 43–62. https://doi.org/10.1016/j.coastaleng.2019.02.004.

Ballio, F., Teruzzi, A., Radice, A., 2009. Constriction effects in clear-water scour at abutments. J. Hydraul. Eng. 135, 140–145.

Breusers, H.N.C., Nicollet, G., Shen, H.W., 1977. Local scour around cylindrical piers. J. Hydraul. Res. 15, 211–252.

Buckingham, E., 1914. On physically similar systems; illustrations of the use of dimensional equations. Phys. Rev. 4, 345.

Carreiras, J., Larroudé, P., Seabra-Santos, F., Mory, M., 2001. Wave scour around piles. Coastal Eng. 2000 1860–1870.

Carrier, G.F., Wu, T.T., Yeh, H., 2003. Tsunami run-up and draw-down on a plane beach. J. Fluid Mech. https://doi.org/10.1017/S0022112002002653.

Carstensen, S., Sumer, B.M., Fredsøe, J., 2010. Coherent structures in wave boundary layers. Part 1. Oscillatory motion. J. Fluid Mech. https://doi.org/10.1017/S0022112009992825.

Chiew, Y.M., 1984. Local Scour at Bridge Piers. the University of Auckland. at Auckland, New Zealand.

Dey, S., Helkjær, A., Mutlu Sumer, B.M., Fredsøe, J., 2011. Scour at vertical piles in sand-clay mixtures under waves. J. Waterw. port, coastal. Ocean Eng. 137, 324–331.

Dey, S., Sumer, B.M., Fredsøe, J., 2006. Control of scour at vertical circular piles under waves and current. J. Hydraul. Eng. 132, 270–279.

Fredsøe, J., Deigaard, R., 1992. Mechanics of Coastal Sediment Transport. World Scientific.

Fuhrman, D.R., Fredsoe, J., Sumer, B.M., 2009a. Bed slope effects on turbulent wave boundary layers: 1. Model validation and quantification of rough-turbulent results. J. Geophys. Res. Ocean. https://doi.org/10.1029/2008JC005045.

Fuhrman, D.R., Fredsøe, J., Sumer, B.M., 2009b. Bed slope effects on turbulent wave boundary layers: 2. Comparison with skewness, asymmetry, and other effects. J. Geophys. Res. Ocean. https://doi.org/10.1029/2008JC005053.

Fuhrman, D.R., Schløer, S., Sterner, J., 2013. RANS-based simulation of turbulent wave boundary layer and sheet-flow sediment transport processes. Coast. Eng. 73, 151–166. https://doi.org/10.1016/j.coastaleng.2012.11.001.

Haddorp, R., 2005. Predictability of Scour at Large Piles Due to Waves and Currents.

Harris, J.M., Whitehouse, R.J.S., Benson, T., 2010. The time evolution of scour around offshore structures. In: Proceedings of the Institution of Civil Engineers-Maritime Engineering. pp. 3–17.

Kader, B.A., Yaglom, A.M., 1991. Spectra and correlation functions of surface layer atmospheric turbulence in unstable thermal stratification. In: Turbulence and Coherent Structures. Springer, pp. 387–412.

Kader, B.A., Yaglom, A.M., Chiew, Y.M., Katul, G.G., Chu, C.R., Parlange, M.B., Albertson, J.D., Ortenburger, T.A., Kolmogorov, A.N., Fomin, S.V., Hager, W.H., Unger, J., Oliveto, G., Ballio, F., Teruzzi, A., Radice, A., 2002. Pier and abutment scour-new laboratory data. First Int. Conf. Scour Found. Novemb. 17-20, 2002, Coll. Station. USA 135, 774–784.

Katsui, H., Toue, T., 1989. Inception of sand motion around a large obstacle. Coast. Eng. 1280–1294. 1988.

Katsui, H., Toue, T., others, 1993. Methodology of estimation of scouring around large-scale offshore structures. In: The Third International Offshore and Polar Engineering Conference.

Katul, G.G., Chu, C.R., Parlange, M.B., Albertson, J.D., Ortenburger, T.A., 1995. Low-wavenumber spectral characteristics of velocity and temperature in the atmospheric surface layer. J. Geophys. Res. Atmos. 100, 14243–14255.

Kim, C.-J., Iwata, K., Miyaike, Y., Yu, H.-S., 1995. Topographical change around multiple large cylindrical structures under wave actions. Coastal Eng. 1994 1212–1226.

Kobayashi, T., 1993. 3-d analysis of flow around a vertical cylinder on a scoured bed. In: Proceedings of the Coastal Engineering Conference. https://doi.org/10.1061/9780872629332.264.

Kobayashi, T., Oda, K., 1995. Experimental study on developing process of local scour around a vertical cylinder. In: Proceedings of the Coastal Engineering Conference. https://doi.org/10.1061/9780784400890.094.

Kolmogorov, A.N., Fomin, S.V., 1961. Elements of the Theory of Functions and Functional Analysis.

Larsen, B.E., Fuhrman, D.R., Baykal, C., Sumer, B.M., 2017. Tsunami-induced scour around monopile foundations. Coast. Eng. 129, 36–49.

McGovern, D.J., Todd, D., Rossetto, T., Whitehouse, R.J.S., Monaghan, J., Gomes, E., 2019. Experimental observations of tsunami induced scour at onshore structures. Coast. Eng. 152, 103505.

Nakamura, T., Kuramitsu, Y., Mizutani, N., 2008. Tsunami scour around a square structure. Coast Eng. J. 50, 209–246.

Pizarro, A., Manfreda, S., Tubaldi, E., 2020. The science behind scour at bridge foundations: a review. Water 12, 374.

Qi, W.-G., Gao, F.-P., 2014. Physical modeling of local scour development around a large-diameter monopile in combined waves and current. Coast. Eng. 83, 72–81.

Raaijmakers, T., Rudolph, D., 2008. Time-dependent scour development under combined current and waves conditions-laboratory experiments with online monitoring technique. In: Proc. 4th Int. Conf. Scour Erosion. ICSE, Tokyo, pp. 152–161.

Rance, P.J., 1980. The potential for scour around large objects. Scour Prev. Tech. around offshore Struct. 41–53.

Sogut, E., 2021. Wave and Current Interactions with Sharp-Edged Beachfront Structures on Rigid and Erodible Berms. State University of New York at Stony Brook.

Sogut, E., Farhadzadeh, A., 2020. Scouring and loading of idealized beachfront building during overland flooding. Coast. Eng. Proc. 7.

Sogut, E., Hsu, T.-J., Farhadzadeh, A., 2022. Experimental and numerical investigations of solitary wave-induced non-equilibrium scour around structure of square cross-section on sandy berm. Coast. Eng. 173, 104091.

Sogut, E., Velioglu Sogut, D., Farhadzadeh, A., 2020. Overland wave propagation and load distribution among arrays of elevated beachfront structures. J. Waterw. Port, Coast. Ocean Eng. 146, 04020016. https://doi.org/10.1061/(ASCE)WW.1943-5460.0000579.

Sogut, E., Velioglu Sogut, D., Farhadzadeh, A., 2019. Effects of building arrangement on flow and pressure fields generated by a solitary wave interacting with developed coasts. Adv. Water Resour. 134, 103450. https://doi.org/10.1016/j.advwatres.2019.103450.

Soulsby, R., 1997. Dynamics of Marine Sands: a Manual for Practical Applications. Thomas Telford.

Soulsby, R.L., Whitehouse, R.J., 1997. Threshold of sediment motion in coastal environments. In: Proc. Pacific Coasts Ports 1997 Conf.

Sumer, B.M., 2007. Mathematical modelling of scour: a review. J. Hydraul. Res. 45, 723–735.

Sumer, B.M., Christiansen, N., Fredsoe, J., 1992a. Time scale of scour around a vertical pile. In: The Second International Offshore and Polar Engineering Conference. International Society of Offshore and Polar Engineers.

Sumer, B.M., Christiansen, N., Fredsøe, J., 1993. Influence of cross section on wave scour around piles. J. Waterw. Port, Coast. Ocean Eng. 119 (5), 477. https://doi.org/10.1061/(ASCE)0733-950X(1993)119:5(477).

Sumer, B.M., Fredsøe, J., 2002. The mechanics of scour in the marine environment. Adv. Ser, Ocean Eng.

Sumer, B.M., Fredsøe, J., 2001a. Wave scour around a large vertical circular cylinder. J. Waterw. Port, Coast. Ocean Eng. 127, 125–134.

Sumer, B.M., Fredsøe, J., 2001b. Scour around pile in combined waves and current. J. Hydraul. Eng. 127, 403–411.

Sumer, B.M., Fredsøe, J., 1997. Hydrodynamics Around Cylindrical Structures, p. 530. pp. xviii+.

Sumer, B.M., Fredsøe, J., Christiansen, N., 1992b. Scour around vertical pile in waves. J. Waterw. port, coastal. Ocean Eng. 118, 15–31.

Sumer, B.M., Fuhrman, D.R., 2020. Turbulence in coastal and civil engineering. In: Advanced Series on Ocean Engineering. https://doi.org/10.1142/9789813234314_fmatter.

Sumer, B.M., Hatipoglu, F., Fredsøe, J., 2007. Wave scour around a pile in sand, medium dense, and dense silt. J. Waterw. Port, Coast. Ocean Eng. 133 (1), 14. https://doi.org/10.1061/(ASCE)0733-950X(2007)133:1(14).

Sumer, B.M., Jensen, P.M., Sørensen, L.B., Fredsøe, J., Liu, P.L.-F., Carstensen, S., 2010. Coherent structures in wave boundary layers. Part 2. Solitary motion. J. Fluid Mech. 646, 207–231.

Toue, T., Katsui, H., Nadaoka, K., 1993. Mechanism of sediment transport around a large circular cylinder. Coastal Engineering 1992 2867–2878.

Velioglu Sogut, D., Sogut, E., Farhadzadeh, A., 2021. Interaction of a solitary wave with an array of macro-roughness elements in the presence of steady currents. Coast. Eng. 164, 103829. https://doi.org/10.1016/j.coastaleng.2020.103829.

Welzel, M., Schendel, A., Hildebrandt, A., Schlurmann, T., 2019. Scour development around a jacket structure in combined waves and current conditions compared to monopile foundations. Coast. Eng. 152, 103515.

Whitehouse, R., 1998. Scour at Marine Structures: A Manual for Practical Applications. Thomas Telford.

Whitehouse, R.J.S., 2004. Marine scour at large foundations. In: Proceedings of the Second International Conference on Scour and Erosion. pp. 455–463. Singapore.

Williams, I.A., Fuhrman, D.R., 2016. Numerical simulation of tsunami-scale wave boundary layers. Coast. Eng. 129, 36–49.

Zanke, U.C.E., Hsu, T.-W., Roland, A., Link, O., Diab, R., 2011. Equilibrium scour depths around piles in noncohesive sediments under currents and waves. Coast. Eng. 58, 986–991.